NeuroImage 59 (2012) 389–398

Contents lists available at ScienceDirect

NeuroImage

journal homepage: www.elsevier.com/locate/ynimg

Prospective and retrospective motion correction in diffusion magnetic resonance imaging of the human brain

Tobias Kober [a,b,c,*], Rolf Gruetter [a,b,d], Gunnar Krueger [c]

[a] Laboratory for Functional and Metabolic Imaging, École Polytechnique Fédérale de Lausanne, Switzerland
[b] Department of Radiology, Centre Hospitalier Universitaire Vaudois and University of Lausanne, Switzerland
[c] Siemens Schweiz AG, Healthcare Sector IM&WS S, Renens, Switzerland
[d] Department of Radiology, University of Geneva, Switzerland

ARTICLE INFO

Article history:
Received 25 February 2011
Revised 1 July 2011
Accepted 4 July 2011
Available online 13 July 2011

Keywords:
MRI
DTI
HARDI
Motion detection
FID navigators
Brain imaging
Multi-coil arrays

ABSTRACT

Diffusion-weighting in magnetic resonance imaging (MRI) increases the sensitivity to molecular Brownian motion, providing insight in the micro-environment of the underlying tissue types and structures. At the same time, the diffusion weighting renders the scans sensitive to other motion, including bulk patient motion. Typically, several image volumes are needed to extract diffusion information, inducing also inter-volume motion susceptibility. Bulk motion is more likely during long acquisitions, as they appear in diffusion tensor, diffusion spectrum and q-ball imaging. Image registration methods are successfully used to correct for bulk motion in other MRI time series, but their performance in diffusion-weighted MRI is limited since diffusion weighting introduces strong signal and contrast changes between serial image volumes.

In this work, we combine the capability of free induction decay (FID) navigators, providing information on object motion, with image registration methodology to prospectively – or optionally retrospectively – correct for motion in diffusion imaging of the human brain. Eight healthy subjects were instructed to perform small-scale voluntary head motion during clinical diffusion tensor imaging acquisitions.

The implemented motion detection based on FID navigator signals is processed in real-time and provided an excellent detection performance of voluntary motion patterns even at a sub-millimetre scale (sensitivity $\geq$ 92%, specificity $>$ 98%). Motion detection triggered an additional image volume acquisition with $b = 0$ s/mm^2 which was subsequently co-registered to a reference volume. In the prospective correction scenario, the calculated motion-parameters were applied to perform a real-time update of the gradient coordinate system to correct for the head movement.

Quantitative analysis revealed that the motion correction implementation is capable to correct head motion in diffusion-weighted MRI to a level comparable to scans without voluntary head motion. The results indicate the potential of this method to improve image quality in diffusion-weighted MRI, a concept that can also be applied when highest diffusion weightings are performed.

Introduction

Diffusion-weighted magnetic resonance imaging (DW-MRI) has become a valuable tool for the investigation and diagnosis of various diseases. Enabling unprecedented insight into brain anatomy, it opens up new perspectives for brain and body imaging, most prominently for the diagnosis of acute stroke (Kloska et al., 2010). It is also increasingly used to investigate other pathologies, including cancer (Charles-Edwards and deSouza, 2006), neurological diseases like multiple sclerosis (Filippi and Agosta, 2010) and impairments in other parts of the body (Koh and Collins, 2007). The capability to visualise the directionality of diffusion through diffusion tensor imaging (DTI, Basser et al., 1994) allows, in conjunction with tractography, more detailed investigation of the brain's architecture and integrity. High angular resolution diffusion imaging (HARDI) methods like q-ball (Callaghan and Xia, 1991; Tuch, 2004) and diffusion spectrum imaging (Tuch et al., 2002; Wedeen et al., 2005) have been used to further improve the precision to measure and visualise complex white matter architecture; however, at a cost. The required employment of up to several hundred diffusion encoding directions lengthens the scan times, consequently increasing the probability that subject motion will occur during the acquisition.

The sensitivity of diffusion imaging to stochastic Brownian motion of free water molecules in the micrometre range also implies an extreme susceptibility to macroscopic or bulk motion of the object being imaged (Tijssen et al., 2009). To extract information on diffusion, the image volume has to be sampled numerous times using different diffusion encoding directions and weightings. This renders diffusion imaging also prone to inter-shot motion.

* Corresponding author at: Ecole Polytechnique Fédérale de Lausanne, LIFMET-CIBM, Station 6, 1015 Lausanne, Switzerland. Fax: +41 21 69 37960.
E-mail address: tobias.kober@epfl.ch (T. Kober).

1053-8119/$ – see front matter © 2011 Elsevier Inc. All rights reserved.
doi:10.1016/j.neuroimage.2011.07.004

Similar to DW-MRI experiments, functional MRI (fMRI) also acquires series of brain volumes and therefore faces similar motion problems arising from patient head movements during the acquisition. Established image registration methods (retro- and prospectively, see Friston et al., 1995; Thesen et al., 2000; Ward et al., 2000), however, cannot be directly applied to diffusion images. The low signal-to-noise ratios (SNR) and the changing contrasts due to the different diffusion encoding directions and weightings hamper the co-registration or even render it impossible at higher diffusion weightings. Motion susceptibility of diffusion MRI hence remains an open issue.

Different approaches have been proposed to mitigate motion artefacts. Post-processing techniques can help to improve the data quality retrospectively. Rejecting outliers in a diffusion dataset (Chang et al., 2005), optimised gradient optimisation schemes for partial datasets (Dubois et al., 2006), and retrospective corrections (Atkinson et al., 2000; Miller and Pauly, 2003; Rohde et al., 2004) have all been shown to increase the quality of corrupted diffusion imaging series.

One can also improve diffusion acquisition techniques. The use of bipolar gradient schemes reduces susceptibility to motion as well as to eddy currents and is widely employed (Prasad and Nalcioglu, 1991). The use of motion-insensitive sampling strategies, such as Turboprop/PROPELLER (Pipe, 1999; Pipe and Zwart, 2006), which was also implemented with a simultaneous parallel imaging reconstruction (Liu et al., 2005), can be used to mitigate motion artefacts. Another straightforward approach is the expedition of the measurement itself, explaining that most diffusion scans are performed using single-shot EPI. In addition, new techniques attempt to reduce overall scan time by introducing parallel imaging to the slice direction (Breuer et al., 2005; Setsompop et al., 2010). Others apply non-Nyquist-obeying radial acquisitions along with constraint reconstruction techniques (Alexander et al., 2006; Mistretta, 2009) or simultaneously refocused EPI sequences in conjunction with parallel imaging in slice direction (Feinberg et al., 2002, 2010). Although all these approaches attempt to reduce the likeliness or the impact of motion in diffusion MRI, they do not remedy its effects.

External devices have also been proposed to track and correct head motion (Forman et al., 2010; Qin et al., 2009; Zaitsev et al., 2006). Once set up, these techniques may provide very precise motion information up to the micrometre scale. They necessitate, however, elaborate experimental skills and a sophisticated setup. Landmarks, typically markers attached to the skin or bite bars, have to be applied to track the movements. This renders the clinical application of those techniques more difficult.

Furthermore, navigator data have been used to detect and correct for motion in diffusion imaging, in particular for segmented turbo spin-echo (de Crespigny et al., 1995; Dietrich et al., 2000; Ordidge et al., 1994) or interleaved EPI (Bammer et al., 2002; Butts et al., 1996, 1997; Nunes et al., 2005) diffusion acquisitions to reduce incoherencies between the segments. Navigator-based motion monitoring has also been implemented in real-time (Porter and Heidemann, 2009; Weih et al., 2004). A similar technique uses spiral trajectories to oversample k-space and gain information about motion and phase errors (Liu et al., 2004). Also, generic MRI motion navigator techniques as floating (Kadah et al., 2004), orbital (Fu et al., 1995), spherical (Welch et al., 2002), spiral (White et al., 2010) or cloverleaf (van der Kouwe et al., 2006) navigators can be employed for diffusion imaging. These techniques are however either restricted to 3D acquisitions or would increase the minimally achievable echo time considerably, which is both disadvantageous for diffusion imaging.

More recently, free induction decay (FID) navigators, which monitor the k-space centre without any spatial encoding, have gained interest. First employed for mitigating respiration- and system-induced B_0 shifts (Hu and Kim, 1994; Pfeuffer et al., 2002), they have also been employed for shimming (Splitthoff and Zaitsev, 2009). Brau and Brittain proposed to use the navigator's DC component to monitor chest motion for gating abdominal acquisitions (Brau and Brittain, 2006); we have previously utilised them to detect head motion in anatomical imaging (Kober et al., 2011).

This work aims at combining the properties of FID motion detection navigators with traditional image registration methods. Our goal was to establish an optimised diffusion acquisition scheme that detects motion, updates the gradient coordinate system in real-time to correct for the motion, and includes an automatic repetition of the motion-corrupted diffusion weighted volumes.

Theory

Coil arrays have become essential components of a modern clinical MRI scanner (Roemer et al., 1990). Ideally, they overcome the limited spatial sensitivity of a single local surface coil by surrounding the imaged object with an array of small coil elements to provide the superior SNR properties of surface coils. Due to a local coil element's steep spatial sensitivity profile, the received signal magnitude and phase may change significantly when the object's position is varied with respect to the coil. This property is exploited for head motion detection in the presented work. For a single-coil-element, the relationship between distance and signal strength can be calculated by means of the laws of electromagnetism. In a realistic in vivo experiment, however, various complicating factors (loading, head geometry, coil coupling and others) render an analytical approach unfeasible. Hence, our detection method is derived from experimental data.

In our experiments, we use a product 32-channel head coil array (based on (Wiggins et al., 2006)). The helmet design of this RF coil ensures close coverage of the subject's head and favours the detection of head movements as outlined above. During the course of the imaging sequence, a short period of free induction decay is repetitively sampled with every coil element after the RF excitation pulse preceding the diffusion-encoding. The placement before the diffusion-encoding ensures insensitivity to diffusion-related contrast changes. A real-time algorithm monitors the FID data over time, comparing the current FID's amplitude and phase with those of an earlier FID. Motion is detected if the FID signal change exceeds an empirical determined threshold. In the presented implementation, an additional imaging volume without diffusion encoding is inserted and registered to a reference volume to characterise the occurred motion. An optional procedure can subsequently be triggered to prospectively correct for the subject motion.

Materials and methods

Sequence modifications

The short FID readout was added after the slice re-winder of the first RF pulse in a twice-refocused spin echo diffusion-weighted EPI sequence (see Fig. 1). The number of acquired data points and the readout bandwidth of the FID navigator were matched to the settings of the imaging readouts, sampling 168 points with each TR and coil element (twice the matrix size, due to automatic oversampling in frequency direction).

To incorporate the additional FID readout, the readout pre-winder gradient pulses and the slice re-winder had to be separated. Consequently, the implementation resulted in a slightly increased echo time (TE) of approximately 1 ms compared to the product diffusion imaging sequence.

Motion detection algorithm and data flow

Incoming FID navigator data were processed using the real-time feedback framework of the scanner's image processing environment. Navigator data from the first volume were used to identify slices with less than 20% of the maximal measured slice energy, i.e. the absolute integral of the strongest coil element in a slice. This simple threshold

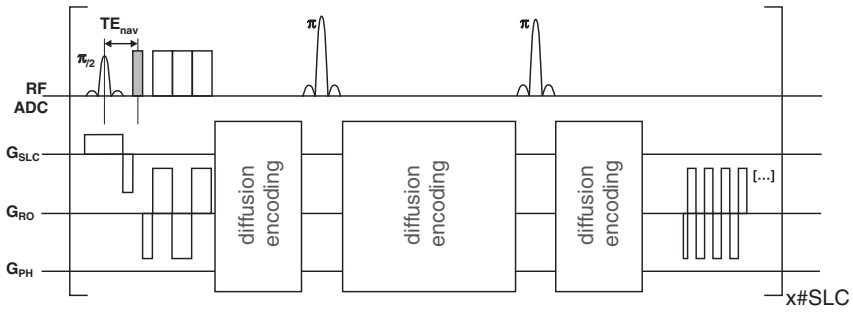

Fig. 1. Schematic sequence diagram depicting one (slice-) repetition of the employed bipolar diffusion sequence. The FID navigator readout (grey) is placed after the slice re-winder, sampling the FID for 1 ms with the employed protocol. The navigator echo time TE_{nav} was 2.2 ms in the study protocol. The FID is sampled in each slice, obtaining information from all coil elements. These data are volume-wise combined with the algorithm presented in the text.

criterion allowed excluding slices that were positioned outside the head, i.e. in the background noise or the neck. The first two slices (in acquisition order) of a volume were discarded in the successive motion detection steps to decrease FID noise arising from residual eddy current history influences. The numbers of all other slices were stored in the set *UsedSlices*.

In each repetition n, the complex average over the sampled navigator data of each slice s ($s \in UsedSlices$) and each coil element c is calculated, $nav_n(s,c)$. The normalised real-valued difference to the preceding navigator is defined as

$$\Delta_n(s,c) = Re\left(\frac{nav_n(s,c) - nav_{n-1}(s,c)}{nav_{n-1}(s,c)}\right)$$

Taking the real value instead of the magnitude ensured the preservation of the signs for the median operation further down. Starting from volume $n \geq 3$, the relative difference $rd(n)$ is calculated from all navigator differences $\Delta_n(s,c)$ using the following heuristic formula:

$$rd(2) = \left\langle max_5^{slices} \left\{ abs\left[median^{coils}(\Delta_2(s,c)) \right] \right\} \right\rangle$$

$$rd(n) = \left\langle max_5^{slices} \left\{ abs\left[median^{coils}(\Delta_n(s,c)) \right] \right\} \right\rangle - rd(2)$$

In words, the median over all coil element signals $\Delta(s, c = 1 \ldots 32)$ is determined for each slice s. Choosing the median instead of the mean here proofed to render the algorithm more robust against outliers. Thus, a list of median difference values of all used slices is obtained. Subsequently, the mean over the five largest absolute differences is calculated. This avoids that a motion occurring late within a repetition is not detected because the very low difference values from the slices before the motion overcast the ones after the motion. At the same time, it is assumed that the head position was different to the preceding repetition in at least five slices. Lastly, the first available difference, $rd(2)$, was used to remove systematic offsets. Note that this assumes that no motion occurred between repetition one and two.

The diagram in Fig. 2 details the data flow of the algorithm. If $rd(n)$ exceeded the empirical threshold of 1%, a trigger signal was transmitted to the sequence. Upon reception of this trigger, an additional acquisition of an entire image volume without diffusion weighting but otherwise identical sequence parameters (herein referred to as 'extra-b0 scan') is inserted after the motion-corrupted volume. The extra-b0 scan was subsequently registered in real-time using the rigid-body registration algorithm available for the fMRI motion-correction framework on the scanner (Thesen et al., 2000). The prospective adaptation of slice positions following head motion may lead to a change in the reference FID signal. To avoid false triggering, navigator data of the first two volumes after an extra-b0 trigger are ignored.

The algorithm can be run in retrospective or prospective mode. In retrospective mode, the co-registration results, i.e. the motion parameters, are stored in a log-file for later correction. In prospective mode, the motion parameters are transmitted back to the sequence, updating the slice positioning to correct for the movement during the measurement.

The calculation time of the registration and the delay of the feedback loop does not always allow for a correction of the volume immediately after the extra-b0 scan. In that case, an additional waiting-b0 scan was automatically added in prospective mode to maintain the magnetisation in steady state.

To further reduce residual motion artefacts in the imaging volume that initiated an extra-b0 volume, the corrupted diffusion encoding step is repeated after the extra-b0 volume (in case of prospective correction, possibly after the waiting-b0 volume). Fig. 3 depicts the acquisition scheme for both the retrospective and prospective case.

Experiments

All experiments were performed on a clinical 3T MRI scanner (Magnetom Trio a Tim System, Siemens Healthcare, Erlangen, Germany) equipped with the product 32-channel receive head coil array (based on Wiggins et al., 2006).

Eight healthy subjects (26 ± 6 years, 4 males and 4 females) were scanned. All subjects provided written informed consent in accordance with the local ethic protocol. The experimental protocol comprised three pairs of diffusion imaging scans in retrospective correction mode. Subjects were briefed to perform small, varying but realistic head movements inside the coil upon verbal instructions. During the first scan of each pair of scans, no verbal movement instructions were given ("rest" scans without motion). In the second scan of each pair, the subjects were asked to move their heads as briefed ("motion" scans). The time points of the verbal commands were randomised between subjects. Eight to ten instructions were issued per series depending on the subject.

The three pairs of scans applied diffusion weightings of $b = 500$, 1000, and 3000 s/mm^2, using the 12-directions product diffusion scheme and five averages (duration of a single scan 5:28 min). Except for the different diffusion weightings, all imaging parameters were identical: TR/TE/TR-Fill = 4800/102/500 ms, matrix size 84×84, FOV 212×212 mm^2, 32 slices of 3 mm thickness, bandwidth = 1384 Hz/pixel and a GRAPPA acceleration factor of two. Employing these parameters, the FID navigator readout duration was 1 ms at an echo time TE_{nav} of 2.2 ms. In addition, one scan was performed in prospective correction mode, i.e. with a prospective update of the gradient coordinate system; this scan was performed using a diffusion weighting with $b = 1000$ s/mm^2. The protocol focused on data acquired in retrospective mode in order to enable comparison of motion-corrupted and motion-corrected images using the same data.

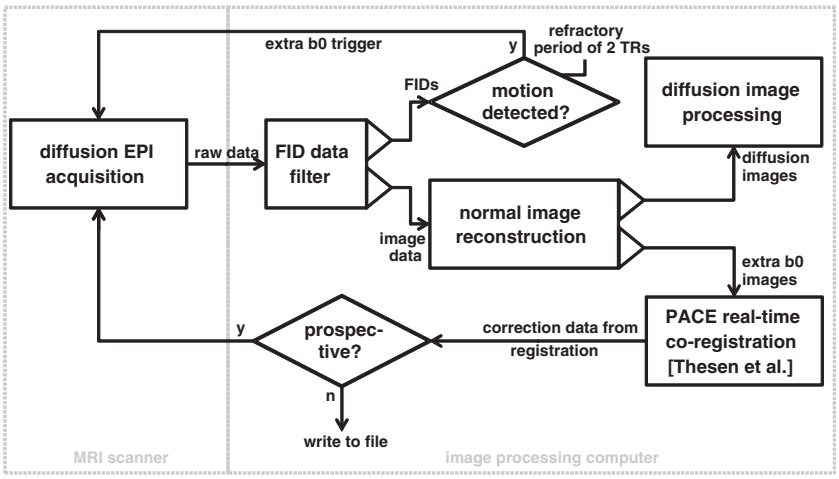

Fig. 2. Data flow diagram of imaging and FID data. At the beginning of the image reconstruction pipeline, the FID data is filtered out and separately processed. If a motion is detected, an extra-b0-scan is triggered using a feedback loop to the sequence. Successively, the image data of this extra-b0-scan is reconstructed normally and then fed in the real-time co-registration module (using the algorithm reported in Thesen et al., 2000). After co-registration, the latter sends the six motion parameters to the sequence, which adapts the gradient system accordingly. In retrospective mode, the motion parameters are written to a file instead.

To assess the stability of the navigator signal, three phantom scans were performed using the same parameters as the human experiments but with ten averages, yielding a scan time of 10:40 min.

Data analysis

Eddy current influence

Despite the use of the eddy current insensitive twice-refocused spin echo diffusion encoding (Reese et al., 2003) we expected the presence of residual eddy current influences on the phase of the FID navigators. To investigate those effects, navigator signals were averaged over all performed phantom scans for each diffusion weighting.

Sensitivity and specificity of the motion detection

The time points of the verbal movement commands were compared with the time points when an extra-b0 scan was triggered during the scan. The resulting number of true and false positive (TP, FP) extra-b0 triggers, as well as the true and false negatives (TN, FN) were combined to give sensitivity (SE) and specificity (SP) measures:

$$SE = \frac{TP}{TP + FN}, \quad SP = \frac{TN}{TN + FP}$$

These measures were calculated from all human experiments and for all diffusion encoding strengths. In addition, a receiver operating characteristic (ROC) analysis was performed to test the power of the detection algorithm for each diffusion weighting. For this purpose, SE and SP figures were calculated for *rd* threshold values from 0% to 20% with a step size of 0.2%. One outcome of this analysis is the optimal threshold, being the intercept of the SE and SP curves (see Fig. 5).

Standard deviation maps

For each pair of scans, the following data were compared: rest scans, motion scans (acquired in retrospective mode) and retrospectively

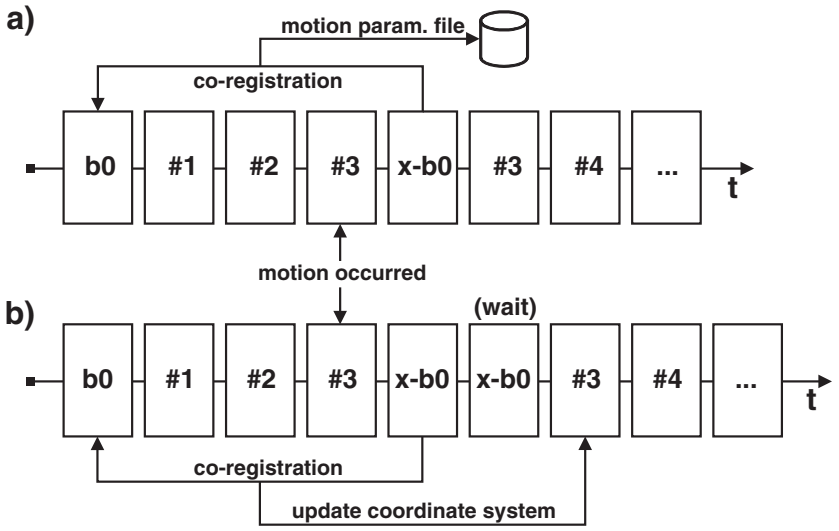

Fig. 3. Scanning schemes in retrospective and prospective mode for the exemplary case that motion is detected in volume #3. The first imaging volume ($b = 0\ s/mm^2$) serves as reference volume for registration. After motion detection, an extra-b0 volume without diffusion encoding is acquired. This volume is co-registered to the reference volume. The obtained motion parameters are either stored (retrospective mode, a) or transmitted back to the sequence to update the gradient coordinate system, i.e. "following" the head movement (prospective mode, b). The registration and feedback typically takes <2 s. Thus, a "waiting-b0-scan" is inserted if necessary. All subsequent scans are acquired with the updated coordinate system including the repetition of the motion-corrupted imaging volume. The latter is also performed in retrospective mode.

corrected motion scans. The latter two use data from the same acquisition, one uncorrected and one corrected retrospectively using the motion parameters calculated but not applied during the scan. For the scan pair acquired with b = 1000 s/mm^2, also the results from the prospective motion correction were available. For a quantitative comparison, averaged magnitude images and standard deviation (SD) maps were calculated for each diffusion direction over the five averages. SD maps were normalised by the greatest SD observed in a patient's set of scans with the same b-value. The averaged magnitude images are expected to show blurring if motion occurred during the measurement. Normalised SD maps were overlaid by using a threshold of 0.25% (see Fig. 7).

Tractography

To illustrate the efficiency of the motion correction, tractography data from a spherical seed region-of-interest (ROI, radius = 2 voxels) located in the frontal part of the corpus callosum was calculated using the Diffusion Toolkit and visualised using TrackVis (Wang et al., 2007). The second-order Runge–Kutta propagation algorithm was employed (angle threshold = 35°) using a FA-based threshold of 0.2 for fibre tracking. Results from scans without motion, with motion, with motion and retrospective correction, and with prospective correction were qualitatively compared. As an indicator of data quality, the mean fibre length in the created tracks was calculated.

Results

Navigator signal stability

Navigator time courses of the phantom scans exhibited good temporal stability and were always below the empirically chosen 1%-threshold. The mean standard deviation of the three phantom experiments (duration 10:40 min) was 0.14% (range 0.13%–0.17%) for b = 500 s/mm^2, 0.19% (range 0.19%–0.20%) and 0.23% (range 0.22%–0.24%) for b = 1000 s/mm^2 and b = 3000 s/mm^2, respectively. Fig. 4a summarises these results and reports the corresponding peak-to-peak values. A regular pattern most likely resulting from residual eddy currents of the diffusion direction scheme was produced. The polarity of the diffusion encoding gradients alternates between averages, explaining why the patterns repeat only every other average. The intensity of the pattern increases with the diffusion encoding strength and is characterised by larger standard deviations and greater peak-to-peak values at higher diffusion weightings (see Fig. 4b). It is important to note that all diffusion-weighted scans were acquired with the same echo-time to ensure comparability between the scans. Consequently, the gradient amplitude is highest in the scans with b = 3000 s/mm^2.

The human rest scans showed similar behaviour with slightly increased noise levels, but remained well below the empirical 1% threshold. The mean standard deviation over the eight experiments was 0.19% (range 0.10%–0.27%) for b = 500 s/mm^2, 0.20% (range 0.11%–0.29%) for b = 1000 s/mm^2 and 0.27% (range 0.19%–0.43%) for b = 3000 s/mm^2.

Motion detection performance

The sensitivity/specificity analysis evidenced that the motion commands and the triggered extra-b0 scans agreed with high sensitivity and specificity. For the experiments in retrospective correction mode, they amounted to SE = 92.0%/SP = 99.8% (b = 500 s/mm^2), SE = 94.6%/SP = 99.6% (b = 1000 s/mm^2) and SE = 93.3%/SP = 98.6% (b = 3000 s/mm^2). The time courses of the rest scans with b = 500 s/mm^2 showed a very low noise level, suggesting that a lower threshold could be applied. The ROC analysis supported this observation. As demonstrated in Fig. 5, the optimal threshold values were 0.83% for the scans with b = 500 s/mm^2, 1.19% and 0.97% for the scans with b = 1000 s/mm^2 and b = 3000 s/mm^2, respectively. The area under the curve (AUC) in the ROC plot revealed an excellent accuracy of the employed detection algorithm for all three diffusion encoding strengths: AUC = 0.91 (b = 500 s/mm^2), AUC = 0.91 (b = 1000 s/mm^2) and AUC = 0.90 (b = 3000 s/mm^2), see Fig. 5.

The motion parameter time courses from the extra-b0 registration revealed that the subjects performed varying motion patterns as instructed, i.e. head shaking, nodding, z-translations and tilts. The medians of the absolute translational (x,y,z) parameters were (1.1/2.8/0.8) mm, with a range of (0–12.1/0–15.7/0–16.7) mm. The respective median of the absolute rotational parameters (rX,rY,rZ) amounted to (1.4/2.1/3.7)°, with a range of (0–16.4/0–26.2/0–30.2)°.

A person cannot perform a precise movement that only affects a single motion parameter. It is therefore not possible to report an absolute detection limit in mm (translation) or degree (rotation); however, even movements on a sub-millimetre range were detected. To illustrate, the motion parameters of the smallest movement which triggered an extra-b0 scan were translations = (0.31/−0.30/0.24) mm and rotations = (−0.13/−0.14/−0.25) degrees. One subject reported that yawning triggered an extra-b0 scan. An exemplary navigator time course together with the obtained motion parameters is shown in Fig. 6.

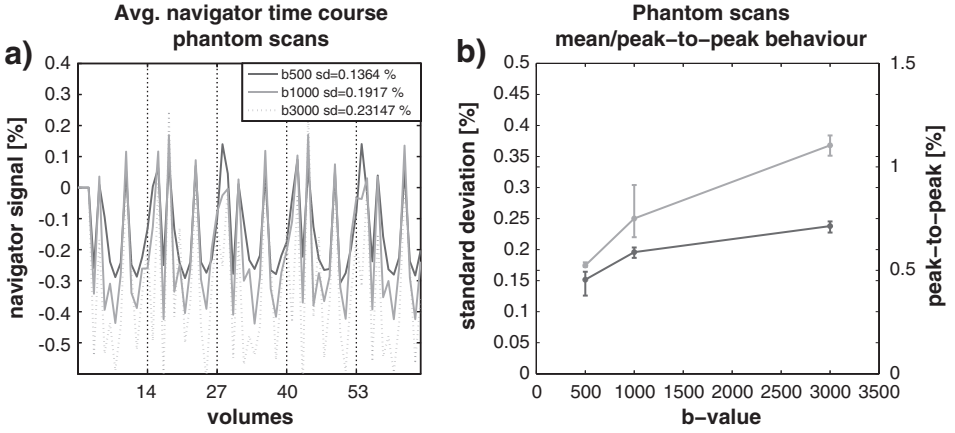

Fig. 4. (a) An excerpt of the averaged navigator time courses of all phantom scans for b = 500, 1000 and 3000 s/mm^2. Vertical lines indicate blocks of one average (b0 + 12 directions, five averages shown). The measurement noise scales with the applied diffusion weighting, which in this case is proportional to the diffusion gradient amplitude. Residual eddy current history effects cause repeated patterns depending on the applied diffusion direction. Odd and even averages show similar behaviour since the bipolar gradient scheme alternates the sign of the diffusion directions with every average. (b) Mean standard deviations and peak-to-peak values are plotted against the applied diffusion weighting; the vertical bars show the observed value ranges over all phantom scans. All figures are given in percent of signal change.

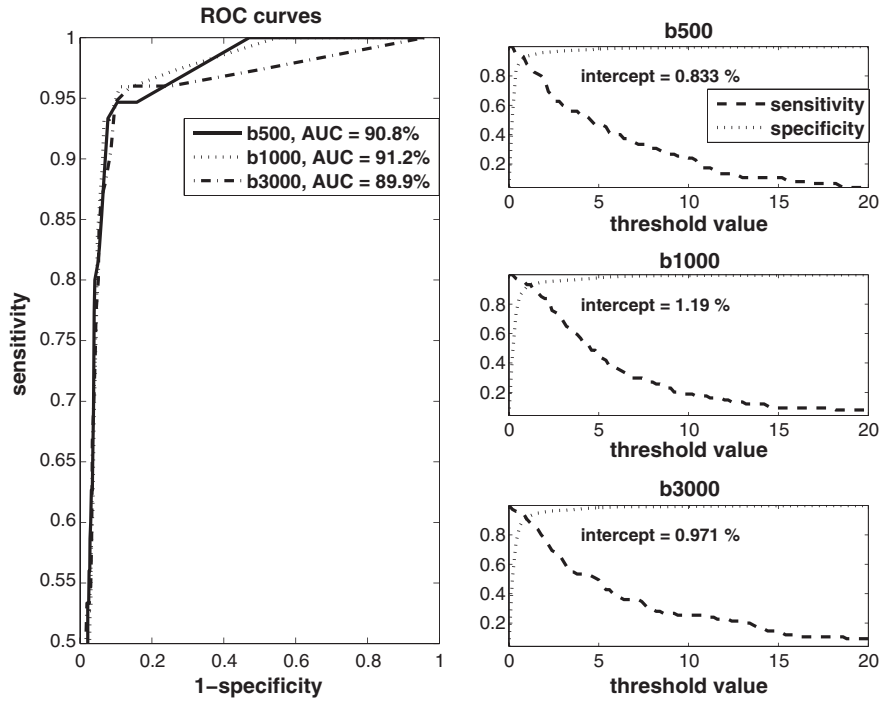

Fig. 5. Receiver operating characteristic analysis using data from all retrospective acquisitions and all subjects (left). The algorithm showed excellent detection performance for all diffusion weightings (area under the curve>90%). The interception between the sensitivity and specificity curve is typically considered the optimal threshold.

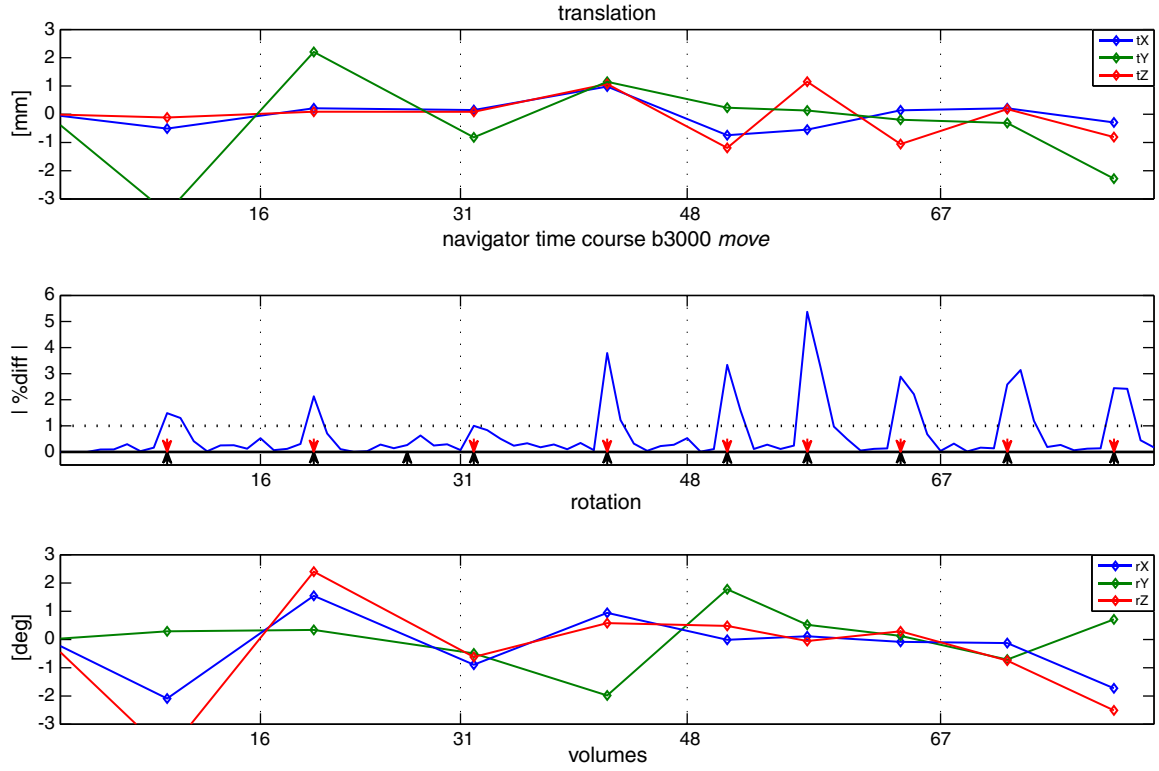

Fig. 6. Example of a motion experiment at b = 3000 s/mm^2. The middle row depicts the navigator time course over the experiment. Vertical lines indicate a block of one average (b0 + 12 directions plus possible extra-b0 volumes); black arrows show when a verbal motion command was issued and red arrows when head motion was detected by the FID navigator algorithm. The upper and lower graphs depict the three translational (top) and the three rotational (bottom) motion parameters revealed by co-registering the extra-b0 scans. Navigator amplitudes do not necessarily scale with motion parameters; which is discussed in Nonlinearity of navigator signal changes and motion parameters. The diagram also shows a case where the navigator signal change was too low to trigger an extra-b0 scan (volume 27).

Resulting diffusion data

The representative dataset in Fig. 7 demonstrates that motion-corrupted datasets exhibit considerable blurring in the averaged magnitude image as well as increased SDs in regions of strong image contrast gradients, e.g. along air-tissue interfaces. On the other hand, both retrospectively and prospectively corrected data show that image quality is well recovered by the correction. Data acquired in prospective mode exhibited increased ghosting in some cases, especially when substantial movements occurred. This is very likely due to changes in the local shim caused by a considerable displacement of the skull cavities.

One should note that in this analysis of the motion-corrupted series the repeated volumes are used (cf. Fig. 3). In a setting without the FID navigators, the volume would of course not be repeated and one would hence obtain worse results than in shown Figs. 7b and 8b.

Tractography

The tractography results confirm the findings obtained with the SD map analysis. Compared to the results from data without motion, the white matter tracts from the seed region in the frontal corpus callosum are greatly reduced in the motion-corrupted dataset (Figs. 8a, b). The retrospectively corrected dataset recovers most of the tracts (Fig. 8c). The prospectively corrected dataset shows very coherent tractography results most similar to the dataset without motion (Fig. 8d).

Discussion

In this work, we propose a motion correction strategy for head diffusion acquisitions. Head motion is detected using FID navigators which have negligible impact on the imaging procedures. The navigators are sampled before the diffusion encoding, rendering them mostly independent of its strength and direction. Additional measurement time is only spent when motion occurs; a non-weighted image volume is acquired and co-registered to a reference volume. The rigid body co-registration provides motion parameters that can be used to align the subsequent diffusion-weighted images retrospectively (retrospective correction mode) or to correct the slice positions in real time (prospective correction mode). To further minimise residual motion artefacts, the acquisition of motion-corrupted volumes is automatically repeated. As a consequence, a motion-corrected dataset with coherent diffusion encoding directions is obtained.

Signal stability and eddy current influences

Both the phantom and the human non-motion scans showed a very stable base line. The employed bipolar gradient scheme ensures negligible impact of eddy current effects on the final image quality. Nevertheless, the analysis revealed an increased noise level with higher diffusion weightings in the sensitive navigator signals, which corresponds to larger diffusion gradient amplitudes in our experiments. The repeatability of the noise patterns suggests residual eddy current effects as the underlying mechanism (see averaged phantom scan navigator signals in Fig. 4).

As mentioned above, an identical echo time was used for all diffusion weightings. This may raise the question whether a clinical DW-MRI scan with $b = 1000\ s/mm^2$ and minimum echo-time would exhibit a noise level comparable to our experiments with $b = 3000\ s/mm^2$. Since eddy currents are not only dependent on the amplitude of the preceding diffusion encoding gradients, but also on the temporal distance between the rising and falling edges of the gradient lobes (partial cancellation of the rising and falling edges), we would expect a very comparable eddy-current performance of the $b = 1000\ s/mm^2$ scans herein and in a clinical protocol with the same diffusion weighting.

Theoretically, prior knowledge of eddy current effects from phantom scans or predictive models could be used to correct for the increased system-related noise levels in the FID time series to detect even more subtle head movements than investigated here. In this context, a simple

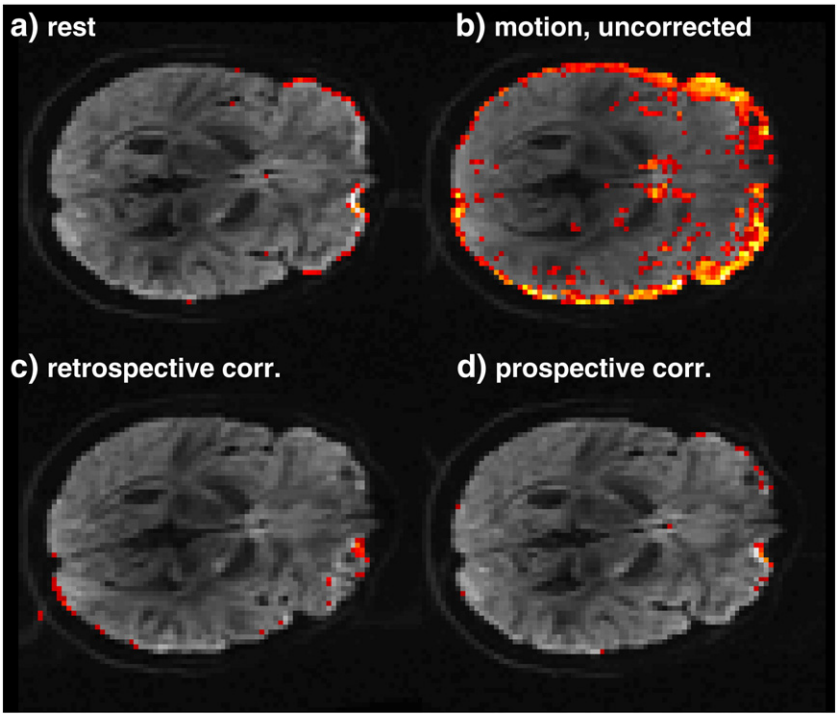

Fig. 7. Representative SD maps overlaid on averaged images of one diffusion direction from a scan with $b = 1000\ s/mm^2$. The corresponding SD maps are normalised with the maximal SD value observed in the four experiments (only normalised SDs > 25% are shown). The first row displays rest (a) and uncorrected motion data (b). The latter exhibits considerable blurring; most of the directional encoding is lost; yet, recovered with the retrospective correction (c). The prospectively corrected dataset (d) shows low SD values and good preservation of the diffusion encoding. Note, only (b) and (c) stem from the same acquisition; it was made sure, however, that the performed movements were comparable.

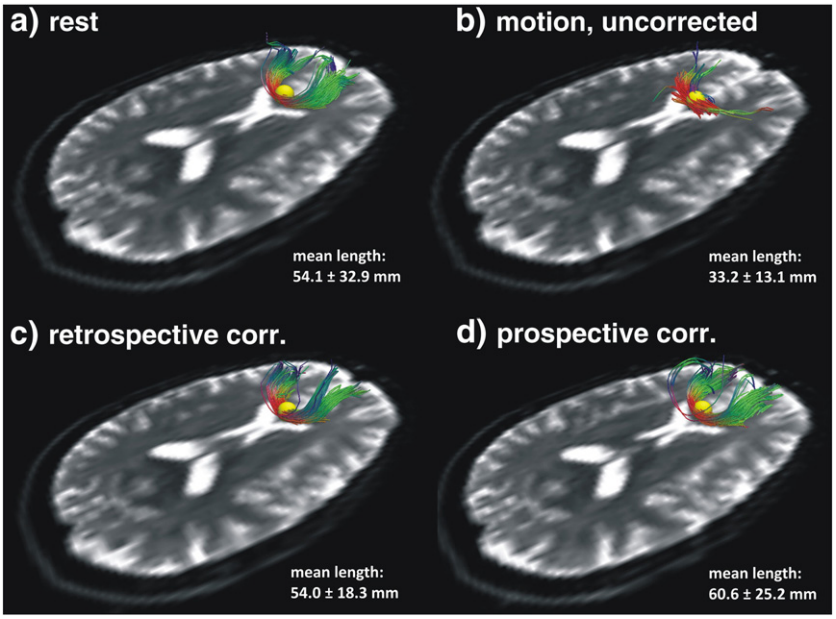

Fig. 8. Tractography results for a seed point (yellow, radius = 2 voxels) placed in the frontal part of the corpus callosum (location anatomically matched). The rest scans shows expected projections in the frontal lobe of the brain (a), whereas in the motion-corrupted dataset a less reasonable tracking result is obtained (b). Retrospective correction using the recorded motion parameters recovers most of the information (c, note that b and c are from the same measurement). The prospectively corrected dataset (d) reveals tracking results very comparable to the reference rest scan and of good quality. The evaluation of the mean lengths of the tracked fibres confirms these observations.

preliminary test in which we subtracted the averaged phantom scan signals from the human rest scans at $b = 3000\ s/mm^2$ revealed a decrease of the average SD by 12.5%.

Accuracy of the motion detection and correction

The FID navigator methodology employed here allows the detection of head movements by comparing two consecutive navigator time points. Although the presented algorithm proved to be able to detect even subtle movements, slow motion – e.g. muscle relaxation after positioning – yielding very small inter-TR position changes might not be discovered. A straightforward remedy would be to compare the current navigator time point with an earlier reference scan in the time series. However, physiological, thermal and other system-related effects may induce a drift in the navigator signal over time. A simple and pragmatic approach addressing this challenge could be the insertion of extra-b0 scans after fixed time intervals, providing regular position updates. The thus obtained additional b0-volumes could also be beneficial for later diffusion data processing.

The motion correction strategy presented here consists of two separate procedures: firstly the motion detection algorithm processing the FID navigators and, secondly, the motion correction by means of image registration. The limits of the motion detection are estimated to be in the sub-voxel range and could potentially be improved by further optimisations including higher channel count. The lower limits of the second step, i.e. the accuracy of the motion correction, are given by the co-registration. The employed algorithm has been demonstrated to provide an accuracy of approx. 10% of the detected motion parameter value (Thesen et al., 2000), i.e. a translation by 1 mm is detected with an accuracy of +/− 0.1 mm. Clinical diffusion imaging applications uses spatial resolutions of 2–3 mm. Thus the estimated capability to correct for sub-millimetres motion patterns allows for correction of clinically relevant motion patterns.

It should be noted that large head movements (>10°, >10 mm) may cause severe local field variations, which may also lead to changes in the level of ghosting artefacts. A more sophisticated solution could automatically trigger a time-consuming shim update or to combine the presented method with the elegant approach of (Ward et al., 2002).

Nonlinearity of navigator signal changes and motion parameters

Although the relative difference in the navigator signal *rd* provides a sensitive measure to detect motion, the *rd* amplitude is not accurately reflecting the amplitudes of the underlying motion parameters. Noteworthy, *rd* measures an integral effect of a dynamically selected subset of slices and coils. Moreover, *rd* considers the complex signal (amplitude and phase), which is sensitive to different underlying effects. Changes in the signal amplitude rather reflect changes in the distance to a coil element, whereas phase effects are more likely to arise from position changes in susceptibility gradients as often seen in air-tissue interfaces.

Furthermore, there are simple geometrical reasons contributing to the nonlinearity. The motion parameters calculated by the co-registration are given with respect to the centre of the image volume. In the local reference frames of the different coil elements, however, small movements (with respect to the centre of the volume) may translate in larger local amplitudes observed in a particular slice and coil.

Timing considerations

The algorithm encompasses two feedback loops between the image reconstruction and the measurement control unit. The first triggers the extra-b0 scans, the second co-registers incoming extra-b0 images and feeds back the motion parameters (prospective mode) or saves the parameters to a log-file (retrospective mode). Since the first feedback loop is embedded in a high-performance environment on the imaging computer, it is very fast. In 99% of the cases, the extra-b0 scan could be performed immediately after motion had been detected.

Another aspect is the length of the navigator readout itself. Here, the readout bandwidth and number of sampling points were matched to that of the imaging readouts only for historic reasons. Notwithstanding, much less points could be sampled; we showed recently that as few as three sample points are sufficient to obtain the same information (Kober et al., 2011), meaning that a sampling duration below 50 μs could be employed to collect motion information. Theoretically, even the three k-space lines acquired for the EPI phase correction (see Fig. 1) could be

used to obtain the same information as from the FID navigators. This would require further investigation on SNR requirements which are beyond the scope of this work; it could, however, eliminate the remaining impact of the FID navigators on the sequence timing, i.e. on the minimal echo time.

Applicable coils

The employed motion detection technique is based on FID signal changes measured with the coil elements of a multi-channel coil array. Assuming cubic coil sensitivity decay, it is probable that the detection performs worse for coils with lower filling factors and a greater distance to the object. The filling factor of the used helmet-shaped coil favoured the presented technique in this respect. However, systematic tests with other coils designs and object geometries will lead to a more detailed understanding for a more generalised application of the developed methodology.

Comparison to purely image-based methods

Image-based motion correction methods for diffusion imaging face the problem of co-registering volumes with different image features due to varying diffusion weightings and directions. In addition, signal intensity decreases with higher diffusion weightings, which further impedes the co-registration. A recent publication by Benner et al. proposed to register image volumes to reference data acquired with the same b-value (instead of registering them to non-weighted volumes), providing a purely image-based prospective correction (Benner et al., 2011). The need for separate reference volumes for each b-value implies that the minimum time for detecting a movement is the time between the current volume and the volume with the same diffusion-weighting contrast. As also stated in the corresponding paper, the approach will fail for higher b-values (data is shown for $b = 700\ s/mm^2$ and $b = 1000\ s/mm^2$) since the image features are too different for an exact registration.

In contrast, it is demonstrated here that FID navigators work reliably for b-values up to $3000\ s/mm^2$. Motion is detected with volume-to-volume time resolution. Moreover, the acquisition of the FID navigator data before signal attenuation due to the diffusion-weighting gradients should allow for motion detection in acquisitions with even higher b-values, probably necessitating an adaptation of the navigator threshold value.

Conclusion

We propose a method that is capable to detect and correct sub-voxel head movements in diffusion-weighted MRI with excellent sensitivity and specificity. A detected head motion triggers a reacquisition of the motion-corrupted image volume in combination with a co-registration technique, enabling retrospective or prospective motion correction. The method promises the potential to reduce the impact of patient motion in clinical exams as well as in research settings also for acquisitions employing high diffusion weightings. We consider it especially useful when scanning unco\operative patient groups such as neurologically impaired or paediatric patients and for long diffusion experiments as required by high angular resolution diffusion imaging techniques.

Acknowledgments

The authors thank José P. Marques and Kieran O'Brien for the numerous fruitful discussions.

This work was supported by the Centre d'Imagerie BioMédicale (CIBM) of the University of Lausanne (UNIL), the Swiss Federal Institute of Technology Lausanne (EPFL), the University of Geneva (UniGe), the Centre Hospitalier Universitaire Vaudois (CHUV), the Hôpitaux Universitaires de Genève (HUG) and the Leenaards and the Jeantet Foundations.

References

Alexander, A., Lee, J., Mistretta, C.A., 2006. Diffusion tensor imaging with highly constrained backprojection (HYPR). Annual Meeting of the ISMRM. ISMRM, Seattle, USA, p. 858.

Atkinson, D., Porter, D.A., Hill, D.L., Calamante, F., Connelly, A., 2000. Sampling and reconstruction effects due to motion in diffusion-weighted interleaved echo planar imaging. Magn. Reson. Med. 44, 101–109.

Bammer, R., Augustin, M., Prokesch, R.W., Stollberger, R., Fazekas, F., 2002. Diffusion-weighted imaging of the spinal cord: interleaved echo-planar imaging is superior to fast spin-echo. J. Magn. Reson. Imaging 15, 364–373.

Basser, P.J., Mattiello, J., LeBihan, D., 1994. MR diffusion tensor spectroscopy and imaging. Biophys. J. 66, 259–267.

Benner, T., van der Kouwe, A.J.W., Sorensen, A.G., 2011. Diffusion imaging with prospective motion correction and reacquisition. Magn. Reson. Med. 65.

Brau, A.C., Brittain, J.H., 2006. Generalized self-navigated motion detection technique: preliminary investigation in abdominal imaging. Magn. Reson. Med. 55, 263–270.

Breuer, F.A., Blaimer, M., Heidemann, R.M., Mueller, M.F., Griswold, M.A., Jakob, P.M., 2005. Controlled aliasing in parallel imaging results in higher acceleration (CAIPIRINHA) for multi-slice imaging. Magn. Reson. Med. 53, 684–691.

Butts, K., de Crespigny, A., Pauly, J.M., Moseley, M., 1996. Diffusion-weighted interleaved echo-planar imaging with a pair of orthogonal navigator echoes. Magn. Reson. Med. 35, 763–770.

Butts, K., Pauly, J., de Crespigny, A., Moseley, M., 1997. Isotropic diffusion-weighted and spiral-navigated interleaved EPI for routine imaging of acute stroke. Magn. Reson. Med. 38, 741–749.

Callaghan, P.T., Xia, Y., 1991. Velocity and diffusion imaging in dynamic NMR microscopy. J. Magn. Reson. 91, 326–352.

Chang, L.C., Jones, D.K., Pierpaoli, C., 2005. RESTORE: robust estimation of tensors by outlier rejection. Magn. Reson. Med. 53, 1088–1095.

Charles-Edwards, E.M., deSouza, N.M., 2006. Diffusion-weighted magnetic resonance imaging and its application to cancer. Cancer Imaging 6, 135–143.

de Crespigny, A.J., Marks, M.P., Enzmann, D.R., Moseley, M.E., 1995. Navigated diffusion imaging of normal and ischemic human brain. Magn. Reson. Med. 33, 720–728.

Dietrich, O., Heiland, S., Benner, T., Sartor, K., 2000. Reducing motion artefacts in diffusion-weighted MRI of the brain: efficacy of navigator echo correction and pulse triggering. Neuroradiology 42, 85–91.

Dubois, J., Poupon, C., Lethimonnier, F., Le Bihan, D., 2006. Optimized diffusion gradient orientation schemes for corrupted clinical DTI data sets. MAGMA 19, 134–143.

Feinberg, D.A., Reese, T.G., Wedeen, V.J., 2002. Simultaneous echo refocusing in EPI. Magn. Reson. Med. 48, 1–5.

Feinberg, D.A., Moeller, S., Smith, S.M., Auerbach, E., Ramanna, S., Glasser, M.F., Miller, K.L., Ugurbil, K., Yacoub, E., 2010. Multiplexed echo planar imaging for sub-second whole brain FMRI and fast diffusion imaging. PLoS One 5, e15710.

Filippi, M., Agosta, F., 2010. Imaging biomarkers in multiple sclerosis. J. Magn. Reson. Imaging 31, 770–788.

Forman, C., Aksoy, M., Hornegger, J., Bammer, R., 2010. Self-encoded marker for optical prospective head motion correction in MRI. Med. Image Comput. Comput. Assist. Interv. 13, 259–266.

Friston, K.J., Ashburner, J., Frith, C.D., Poline, J.B., Heather, J.D., Frackowiak, R.S.J., 1995. Spatial registration and normalization of images. Hum. Brain Mapp. 3, 165–189.

Fu, Z.W., Wang, Y., Grimm, R.C., Rossman, P.J., Felmlee, J.P., Riederer, S.J., Ehman, R.L., 1995. Orbital navigator echoes for motion measurements in magnetic resonance imaging. Magn. Reson. Med. 34, 746–753.

Hu, X., Kim, S.G., 1994. Reduction of signal fluctuation in functional MRI using navigator echoes. Magn. Reson. Med. 31, 495–503.

Kadah, Y.M., Abaza, A.A., Fahmy, A.S., Youssef, A.B., Heberlein, K., Hu, X.P., 2004. Floating navigator echo (FNAV) for in-plane 2D translational motion estimation. Magn. Reson. Med. 51, 403–407.

Kloska, S.P., Wintermark, M., Engelhorn, T., Fiebach, J.B., 2010. Acute stroke magnetic resonance imaging: current status and future perspective. Neuroradiology 52, 189–201.

Kober, T., Marques, J.P., Gruetter, R., Krueger, G., 2011. Head motion detection using FID navigators. Magn. Reson. Med. 66 (1) (Jul), 135–143. doi:10.1002/mrm.22797. (Electronic publication ahead of print 2011 Feb 17).

Koh, D.M., Collins, D.J., 2007. Diffusion-weighted MRI in the body: applications and challenges in oncology. AJR Am. J. Roentgenol. 188, 1622–1635.

Liu, C., Bammer, R., Kim, D.H., Moseley, M.E., 2004. Self-navigated interleaved spiral (SNAILS): application to high-resolution diffusion tensor imaging. Magn. Reson. Med. 52, 1388–1396.

Liu, C., Moseley, M.E., Bammer, R., 2005. Simultaneous phase correction and SENSE reconstruction for navigated multi-shot DWI with non-cartesian k-space sampling. Magn. Reson. Med. 54, 1412–1422.

Miller, K.L., Pauly, J.M., 2003. Nonlinear phase correction for navigated diffusion imaging. Magn. Reson. Med. 50, 343–353.

Mistretta, C.A., 2009. Undersampled radial MR acquisition and highly constrained back projection (HYPR) reconstruction: potential medical imaging applications in the post-Nyquist era. J. Magn. Reson. Imaging 29, 501–516.

Nunes, R.G., Jezzard, P., Behrens, T.E., Clare, S., 2005. Self-navigated multishot echo-planar pulse sequence for high-resolution diffusion-weighted imaging. Magn. Reson. Med. 53, 1474–1478.

Ordidge, R.J., Helpern, J.A., Qing, Z.X., Knight, R.A., Nagesh, V., 1994. Correction of motional artifacts in diffusion-weighted MR images using navigator echoes. Magn. Reson. Imaging 12, 455–460.
Pfeuffer, J., Van de Moortele, P.F., Ugurbil, K., Hu, X., Glover, G.H., 2002. Correction of physiologically induced global off-resonance effects in dynamic echo-planar and spiral functional imaging. Magn. Reson. Med. 47, 344–353.
Pipe, J.G., 1999. Motion correction with PROPELLER MRI: application to head motion and free-breathing cardiac imaging. Magn. Reson. Med. 42, 963–969.
Pipe, J.G., Zwart, N., 2006. Turboprop: improved PROPELLER imaging. Magn. Reson. Med. 55, 380–385.
Porter, D.A., Heidemann, R.M., 2009. High resolution diffusion-weighted imaging using readout-segmented echo-planar imaging, parallel imaging and a two-dimensional navigator-based reacquisition. Magn. Reson. Med. 62, 468–475.
Prasad, P.V., Nalcioglu, O., 1991. A modified pulse sequence for in vivo diffusion imaging with reduced motion artifacts. Magn. Reson. Med. 18, 116–131.
Qin, L., van Gelderen, P., Derbyshire, J.A., Jin, F., Lee, J., de Zwart, J.A., Tao, Y., Duyn, J.H., 2009. Prospective head-movement correction for high-resolution MRI using an in-bore optical tracking system. Magn. Reson. Med. 62, 924–934.
Reese, T.G., Heid, O., Weisskoff, R.M., Wedeen, V.J., 2003. Reduction of eddy-current-induced distortion in diffusion MRI using a twice-refocused spin echo. Magn. Reson. Med. 49, 177–182.
Roemer, P.B., Edelstein, W.A., Hayes, C.E., Souza, S.P., Mueller, O.M., 1990. The NMR phased array. Magn. Reson. Med. 16, 192–225.
Rohde, G.K., Barnett, A.S., Basser, P.J., Marenco, S., Pierpaoli, C., 2004. Comprehensive approach for correction of motion and distortion in diffusion-weighted MRI. Magn. Reson. Med. 51, 103–114.
Setsompop, K., Gagoski, B.A., Polimeni, J.R., Witzel, T., Wedeen, V.J., Wald, L.L., 2010. Blipped CAIPIRHINA for simultaneous multi-slice EPI with reduced g-factor penalty. Joint Annual Meeting of the ISMRM, Stockholm, Sweden, p. 551.
Splitthoff, D.N., Zaitsev, M., 2009. SENSE shimming (SSH): a fast approach for determining B(0) field inhomogeneities using sensitivity coding. Magn. Reson. Med. 62, 1319–1325.
Thesen, S., Heid, O., Mueller, E., Schad, L.R., 2000. Prospective acquisition correction for head motion with image-based tracking for real-time fMRI. Magn. Reson. Med. 44, 457–465.
Tijssen, R.H., Jansen, J.F., Backes, W.H., 2009. Assessing and minimizing the effects of noise and motion in clinical DTI at 3 T. Hum. Brain Mapp. 30, 2641–2655.
Tuch, D.S., 2004. Q-ball imaging. Magn. Reson. Med. 52, 1358–1372.
Tuch, D.S., Reese, T.G., Wiegell, M.R., Makris, N., Belliveau, J.W., Wedeen, V.J., 2002. High angular resolution diffusion imaging reveals intravoxel white matter fiber heterogeneity. Magn. Reson. Med. 48, 577–582.
van der Kouwe, A.J., Benner, T., Dale, A.M., 2006. Real-time rigid body motion correction and shimming using cloverleaf navigators. Magn. Reson. Med. 56, 1019–1032.
Wang, R., Benner, T., Sorensen, A.G., Wedeen, V.J., 2007. Diffusion toolkit: a software package for diffusion imaging data processing and tractography. Int. Soc. Magn. Reson. Med., 15, p. 3720. Berlin, Germany.
Ward, H.A., Riederer, S.J., Grimm, R.C., Ehman, R.L., Felmlee, J.P., Jack Jr., C.R., 2000. Prospective multiaxial motion correction for fMRI. Magn. Reson. Med. 43, 459–469.
Ward, H.A., Riederer, S.J., Jack Jr., C.R., 2002. Real-time autoshimming for echo planar timecourse imaging. Magn. Reson. Med. 48, 771–780.
Wedeen, V.J., Hagmann, P., Tseng, W.Y., Reese, T.G., Weisskoff, R.M., 2005. Mapping complex tissue architecture with diffusion spectrum magnetic resonance imaging. Magn. Reson. Med. 54, 1377–1386.
Weih, K.S., Driesel, W., von Mengershausen, M., Norris, D.G., 2004. Online motion correction for diffusion-weighted segmented-EPI and FLASH imaging. MAGMA 16, 277–283.
Welch, E.B., Manduca, A., Grimm, R.C., Ward, H.A., Jack Jr., C.R., 2002. Spherical navigator echoes for full 3D rigid body motion measurement in MRI. Magn. Reson. Med. 47, 32–41.
White, N., Roddey, C., Shankaranarayanan, A., Han, E., Rettmann, D., Santos, J., Kuperman, J., Dale, A., 2010. PROMO: Real-time prospective motion correction in MRI using image-based tracking. Magn. Reson. Med. 63, 91–105.
Wiggins, G.C., Triantafyllou, C., Potthast, A., Reykowski, A., Nittka, M., Wald, L.L., 2006. 32-channel 3 Tesla receive-only phased-array head coil with soccer-ball element geometry. Magn. Reson. Med. 56, 216–223.
Zaitsev, M., Dold, C., Sakas, G., Hennig, J., Speck, O., 2006. Magnetic resonance imaging of freely moving objects: prospective real-time motion correction using an external optical motion tracking system. NeuroImage 31, 1038–1050.